Unveiling the multiphase fate of 2,4-dinitrophenol on aerosols: Interfacial hydration governs competing oxidation pathways and unexpected toxicity amplification

Chenlei Wang[1], Ran Li[1], Jiaxing Sun[2], Zihan Zhang[1], Nan Zhao[1], Leilei Liu*[1], Zuju Ma[1], Maoxia He[3], Jianfei Sun*[1]

[1]School of Environmental and Material Engineering, Yantai University, Yantai 264005, P. R. China

[2]Shandong Pengbo Safety & Environmental Services Limited, Yantai 265600, P. R. China

[3]Environment Research Institute, Shandong University, Qingdao 266237, P. R. China

Keywords: Phenols; Multi-oxidant; Solvation effect; Density functional theory; Biotoxicity

---

*Corresponding author. E-mail: Jianfei Sun: jianfeisun@ytu.edu.cn

Leilei Liu: liuleileimail@163.com

Abstract

This study elucidates the atmospheric transformation mechanisms of 2,4-dinitrophenol (2,4-DNP) using an integrated computational framework. Initial oxidation by hydroxyl radicals (•OH) and ozone (O_3) was identified as the dominant pathway, whereas the direct reaction with nitrogen dioxide radical (•NO_2) is kinetically hindered. A key mechanistic insight is that these primary reactions are inhibited by solvation effects, while nitro substituents further suppress the reaction rates, establishing a quantitative link between electronic structure and degradation kinetics. The subsequent atmospheric fate of the radical intermediate is governed by hydrogen atom abstraction (HAA) reactions with ambient oxygen (O_2) and •NO_2. Molecular dynamics (MD) simulations demonstrate that the adsorption of 2,4-DNP onto aerosol surrogates is non-monotonically modulated by interfacial hydration. Crucially, computational toxicology predicts that the ozonolysis process amplifies, rather than mitigates, environmental risk by generating secondary products with significantly enhanced mutagenicity and developmental toxicity. These findings provide mechanistic insights into the environmental risk amplification associated with nitroaromatic compounds and highlight the necessity of evaluating toxic transformation products for accurate environmental risk assessment.

1 Introduction

Atmospheric aerosols, as pivotal regulators of the Earth's climate system and environmental quality, have long placed the complex study of their physicochemical processes at the forefront of scientific inquiry(Perumpully and Gautam, 2025; Mcneill, 2017). Among them, secondary organic aerosols (SOAs) exert substantial influences on the global radiation balance and public health(Li et al., 2022a; Kroll and Seinfeld, 2008). Their formation originates from the oxidation, nitration, and subsequent reactions of volatile organic compounds (VOCs), which generate semi-volatile and low-volatility products(Fan et al., 2022; Li et al., 2021; Mahilang et al., 2021). Within the diverse range of precursors, nitrophenolic compounds (NPs) have attracted considerable attention because of their strong light-absorbing properties, inherent biological toxicity, and potential role as important SOA precursors(Li et al., 2022b; Li et al., 2020; Salvador et al., 2021). As a representative nitrated aromatic compound, 2,4-dinitrophenol (2,4-DNP) is widely present in industrial emissions and can also be formed through atmospheric secondary reactions, posing considerable environmental risks(Shukla et al., 2009; Yan et al., 2021).

However, accurately assessing the environmental risks of nitrophenolic pollutants and predicting their fate requires more than identifying their large-scale sources and impacts. The key lies in elucidating their specific chemical transformation mechanisms in the atmosphere. Current understanding of the degradation mechanisms of organic compounds mainly focuses on homogeneous reactions, particularly daytime photochemical oxidation pathways dominated by •OH(Schaefer and Herrmann, 2018; Hu et

al., 2021; Liu et al., 2023). In reality, a significant fraction of atmospheric reactions occurs at the heterogeneous interfaces of aerosols or droplets, a process that is especially crucial at night and under highly polluted conditions(Xing et al., 2019). At these interfaces, the molecular orientation of pollutants, the local solvation environment, particularly the structure of water molecules and interactions with particle surfaces collectively reshape their reactivity and pathways, potentially even dictating their ultimate environmental fate(Ohto et al., 2019; Mao et al., 2024; Lee et al., 2014). Consequently, selecting a model system that can effectively represent the surface characteristics of real atmospheric carbonaceous particles is of great importance. Fullerene (C60), owing to its well-defined, stable carbon cage structure and abundant π-electron cloud, provides an ideal model for studying non-covalent interactions at organic compound-particle interfaces(Athar and Patnaik, 2022; Liu and Lu, 2024). This offers a clear platform for probing the molecular-level regulatory role of interfacial hydration.

In the complex and dynamic real atmosphere, interfacial chemical transformations constitute a competitive and evolving process. A comprehensive understanding of the atmospheric behavior of nitroaromatic compounds requires moving beyond the traditional isolated study of single static oxidation pathways. Instead, it requires a perspective that considers their fate within a dynamic network driven by multiple reactive species(Thangamani et al., 2016). The key drivers of this network are three core atmospheric oxidants whose relative importance varies with environmental conditions(Sun et al., 2021). These include the primary daytime oxidant •OH, O_3 with its high background concentration and strong oxidizing capacity, and •NO_2, which can accumulate at night

in polluted regions and initiate non-photochemical nitration pathways(Delaria and Cohen, 2023; Pillar et al., 2014; Yang et al., 2023b). Differences in the concentrations, reactivities, and reaction mechanisms of these species collectively shape the diverse transformation pathways of nitroaromatics across diurnal cycles and under varying pollution regimes.

Notably, such multi-pathway transformation processes generate a series of intermediates and final products with diverse chemical properties, which can fundamentally alter the ecological risk profile of nitroaromatic pollutants(Tiwari et al., 2019; Tam et al., 2021). Taking 2,4-DNP as an example, it exhibits not only acute toxicity but also potential for bioaccumulation and genotoxicity, thereby posing a long-term ecological threat through food-chain amplification(Ahmaruzzaman et al., 2024; Mangotra and Singh, 2024; Grundlingh et al., 2011). However, traditional experimental approaches often struggle to comprehensively identify all reactive intermediates and transformation products, and are frequently inadequate for efficiently evaluating their toxicological effects(Tam et al., 2021; Vom Eyser et al., 2013).

To address these gaps, this study employs an integrated multiscale theoretical framework combining density functional theory (DFT), molecular dynamics (MD) simulations, and computational toxicology to investigate the competing oxidation and nitration pathways of 2,4-DNP in gas and aqueous phases, its interfacial adsorption behavior on carbonaceous aerosol surrogates under different hydration, and the toxicity evolution of its transformation products. The results provide mechanistic insights into

the multiphase fate of nitrated aromatics and highlight the importance of evaluating toxic intermediates in atmospheric risk assessment.

2 Computational methods

2.1 Density functional theory

All density functional theory calculations in this study were performed using the Gaussian 16 software package(Frisch et al., 2016). Geometry optimization, frequency analysis, and single-point energy calculations were conducted for all structures along the reaction pathway, including reactants (Rs), transition states (TSs), intermediates (IMs), and products (Ps), employing the M06-2X functional(Zhao and Truhlar, 2008). To validate the reliability of the chosen basis set, the representative reaction 2,4-DNP + •OH → IM3 was selected, and reaction energies using multiple basis sets were systematically compared, as summarized in Table S1 of the Supplement. The results indicated that the exothermicity computed with different basis sets are in excellent agreement. Among the tested combinations, M06-2X/6-311++G(3df,2p) level yields reaction energies closest to the high-accuracy CCSD(T) benchmark(Spiegel et al., 2024; Nagy, 2024). Considering both computational accuracy and efficiency, the composite method M06-2X/6-31+G(d,p)//6-311++G(3df,2p) was consistently applied in all subsequent calculations. Transition states were located using the TS optimization algorithm and further validated through vibrational frequency analysis and intrinsic reaction coordinate (IRC) calculations(Maeda et al., 2015). Frequency analysis confirmed that all stable structures exhibit no imaginary frequencies, while each transition state possesses exactly one imaginary frequency, consistent with the characteristics of a first-

order saddle point, thereby validating the reaction pathway. The IRC trajectories for key transition states are shown in Figure S1. In addition, the solvation model based on density (SMD)(Kromann et al., 2018) was employed to analyze the electronic structures, reactive sites, and free energy changes of key molecules in solvated states.

To gain deeper insights into the ground-state electronic structure and the delocalization characteristics of potential reactive sites, orbital-weighted dual descriptor (OWDD)(Pino-Rios et al., 2019) analysis was conducted using the Multiwfn program(Lu and Chen, 2012). Furthermore, the independent gradient model (IGM) approach was employed to systematically examine both chemical bonding and noncovalent weak interactions within the system(Lefebvre et al., 2017; Lu and Chen, 2022).

2.2 Molecular dynamics simulations

All MD simulations were performed using the GROMACS 2018.8 software package(Van Der Spoel et al., 2005). The simulation system was constructed within a periodic boundary box measuring 30 Å × 30 Å × 60 Å. Each system contained 6 C60 molecules and 15 2,4-DNP molecules, solvated with varying numbers of water molecules (100, 200, 300, and 400), using the explicit SPC/E water model. To mimic a realistic aerosol multiphase interface, a 20 Å vacuum layer was introduced along the z-axis to create an explicit air-water interface.

The AMBER99SB-ILDN force field was employed for C60 and water molecules, whereas the generalized AMBER force field (GAFF) was used to parameterize 2,4-DNP(Shirts et al., 2003). All topology files were generated with the interactive sobtop

program(Lu, 2026). Prior to production runs, each system underwent energy minimization to eliminate unfavorable atomic overlaps. The systems were subsequently equilibrated for 500 ps in the NVT ensemble at 298.15 K with a 2 fs integration time step, followed by production MD simulations of 1 ns for data collection and analysis. All molecular visualizations and trajectory analyses were performed using the VMD software(Humphrey et al., 1996).

2.3 Kinetic calculations

The rate constants for the primary reactions were calculated using the thermodynamic formulation of the conventional transition state theory (TST)(Tuñón and Williams, 2019) with support from the KISthelp tool(Canneaux et al., 2014) and TST calculator(Lu, 2025), as represented by the following equation:

$$k^{\mathrm{TST}}=\sigma * k_{\mathrm{B}} T/\mathrm{h} * \mathrm{e}^{-\Delta G \neq /(k_{\mathrm{B}} T)} \quad (1)$$

where σ is the reaction path degeneracy, k_{B} is the Boltzmann constant, T is the temperature, and h is Planck's constant. $\Delta G^{\neq}$ represents the standard Gibbs free energy of activation for the considered reaction. For reaction path simplicity, the following equation is followed:

$$\sigma=\sigma_{rot,\ R}/\sigma_{rot,\ \mathrm{TS}} \quad (2)$$

where $\sigma_{rot,\ R}$ and $\sigma_{rot,\ \mathrm{TS}}$ are rotational symmetry numbers of reactants and transition states (for N molecule reactions, $\sigma_{rot,\ R}$ is the product of the rotational symmetry numbers of all the reactants); σ is generally 1 for reactions of macromolecular systems.

2.4 Computational toxicology

The toxicological profiles of 2,4-DNP and its atmospheric transformation products were characterized through a hierarchical quantitative structure activity relationship (QSAR) strategy(Young et al., 2008). Key toxicity endpoints, including Ames mutagenicity(Sushko et al., 2010) and developmental toxicity(Cassano et al., 2010), were predicted using the Toxicity Estimation Software Tool (T.E.S.T.) version 5.1.2 developed by the U.S. Environmental Protection Agency(Epa, 2020). All predictions were subjected to applicability domain verification based on descriptor leverage analysis, and only data for compounds falling within the chemical space defined by the training set were retained to ensure the statistical validity and reliability of subsequent comparative toxicological analyses(Benfenati et al., 2009).

3 Results and discussion

3.1 Reaction mechanisms of 2,4-DNP with O_3, •OH, and •NO_2 in the gas and aqueous phases

Establishing the stable molecular configuration and regional reactivity of 2,4-DNP is essential for understanding the initial reaction mechanisms with O_3 (an electrophile), •OH (a radical), and •NO_2 (which exhibits both electrophilic and radical characteristics). Such characterization provides critical theoretical insights into the distinct mechanistic origins of these reaction processes. To elucidate the fundamental reaction pathways and selectivity differences of 2,4-DNP with various reactants in multiphase environments, this study initiates a theoretical characterization of its ground state, including its electronic structure and reactive sites.

3.1.1 Characterization of the electronic structure of 2,4-DNP

Based on geometric optimization and electronic structure calculations, the stable conformation of 2,4-DNP and its reactive sites analysis are shown in Figure 1. The global minimum energy conformation stabilized by intramolecular hydrogen bonding is presented in Figure 1a, while the OWDD isosurface in Figure 1b clearly delineates the nucleophilic and electrophilic reaction regions of the molecule, thus providing a robust theoretical foundation for elucidating the subsequent reaction mechanisms.

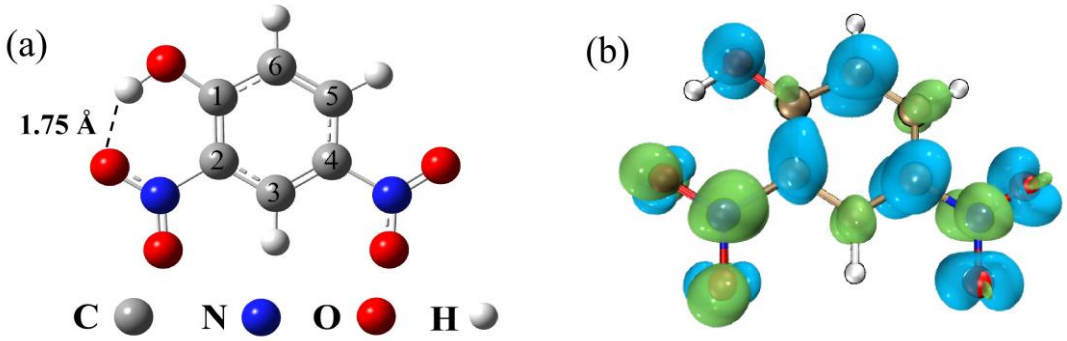


Figure 1 (a) The most stable configuration of 2,4-DNP, stabilized by intramolecular hydrogen bonding. (b) Isosurface of the OWDD for 2,4-DNP, where blue and red regions denote nucleophilic and electrophilic sites, respectively.

The global minimum energy conformation of 2,4-DNP is depicted in Figure 1a, with an electronic energy of −449508.49 kcal mol^{-1}. The exceptional stability of this structure arises primarily from the synergistic effects of intramolecular hydrogen bonding and π-electron delocalization. Structural analysis indicates that a strong intramolecular hydrogen bond (O–H···O–N) between the hydroxyl group and the ortho-positioned nitro group (position 2), with a bond length of 1.75 Å—a value characteristic of strong intramolecular hydrogen bonds (1.6–1.9 Å)(Steiner, 2002). This interaction forms a stable six-membered ring motif, which closely resembles the strain-free chair conformation of cyclohexane and thus provides optimal stabilization(Barton and Cookson,

1956). This hydrogen bond contributes substantial stabilization energy and constitutes the principal factor governing conformational preference. Additionally, both the ortho- and para-nitro groups (at positions 2 and 4, respectively) adopt nearly coplanar orientations relative to the benzene ring, with dihedral angles of 178.30° and 179.67°, approaching the ideal 180° for maximum orbital overlap. Importantly, thereby enabling effective p–π conjugation with the aromatic π system and further enhancing the overall molecular stability(Szatylowicz et al., 2017). Importantly, these two stabilizing factors are mutually reinforcing: the hydrogen bond locks the ortho-nitro group into the plane, facilitating conjugation, while the enhanced conjugation further polarizes the nitro group, strengthening the hydrogen bond.

As shown in Figure 1b, the OWDD isosurface analysis (Δfω) reveals well-defined regional chemical features of the 2,4-DNP. Blue regions ($\Delta f\omega < 0$) are localized around specific carbon atoms on the benzene ring and the hydroxyl oxygen atom, indicating sites rich in lone electron pairs and thus prone to nucleophilic attack These nucleophilic sites arise from the electron-donating effect of the hydroxyl group, which concentrates electron density at the ortho and para positions relative to the nitro groups. In contrast, green regions ($\Delta f\omega > 0$) are mainly located at the outer ends of the oxygen and nitrogen atoms in the nitro and hydroxyl groups, showing electrophilic features associated with σ-hole interactions caused by the polarization of N–O and O–H bonds. This electronic structure feature provides a relia a reliable prediction for predicting its reactivity toward various atmospheric oxidants. As a strong electrophile, O_3 preferentially targets the electron-rich carbon atoms (blue regions), initiating electrophilic addition at the sites

with the highest nucleophilic character. Meanwhile, •OH displays dual reactivity: it adds to nucleophilic blue regions on the benzene ring, while also abstracting hydrogen atoms from weakly electrophilic sites such as the C–H bonds (adjacent to nitro groups) or the hydroxyl hydrogen, which correspond to regions of weaker Δfω positive values. Similarly, $•NO_2$, possessing both radical and electrophilic characteristics, displays dual reactivity, participating either in radical addition to nucleophilic carbons or in hydrogen abstraction reactions, with its preference modulated by the local Δfω distribution.

3.1.2 Primary reactions of 2,4-DNP with O_3, •OH, and $•NO_2$

Based on the analysis of nucleophilic and electrophilic sites in the electronic structure of 2,4-DNP, this section systematically elaborates the primary reaction pathways of 2,4-DNP with O_3, •OH, and $•NO_2$. The competition among different channels is elucidated through thermodynamic and kinetic calculations, thereby revealing transformation mechanisms of 2,4-DNP in the atmosphere.

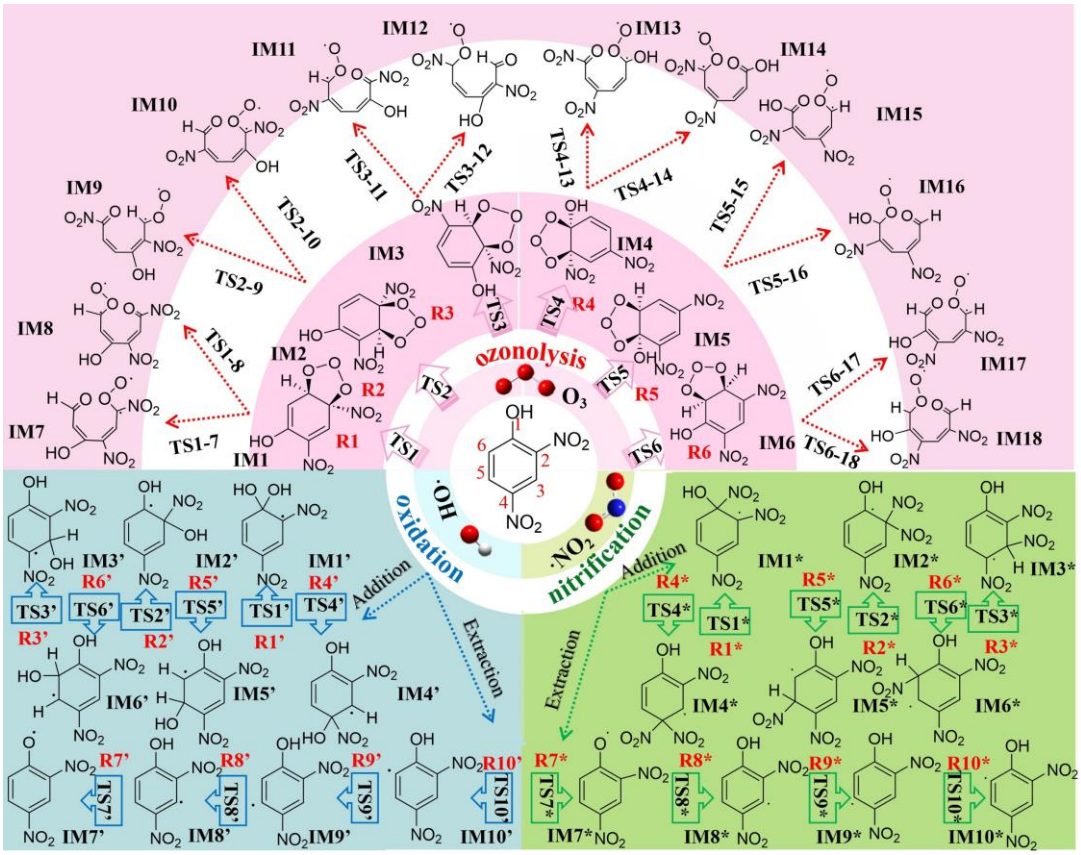


Figure 2 Proposed initial reaction mechanisms of 2,4-DNP with O_3, •OH, and •NO_2.

The coexistence of an electron-donating hydroxyl group and strong electron-withdrawing nitro groups in the 2,4-DNP induces a highly polarized and asymmetric distribution of π-electron density in the benzene ring(Li et al., 2023). This distinct electronic structure directly governs the pronounced regioselectivity of its reactions with O_3, •OH, and •NO_2.

As a typical 1,3-dipole, ozone can attack the electron-rich aromatic π-system via cycloaddition. Calculations indicate that among the six possible 1,3-dipolar cycloaddition pathways, the reaction preferentially occurs at the C5–C6 bond located between the hydroxyl and nitro groups, as indicated by the red region in Figure 2. The reaction proceeds via transition state TS6, in which the terminal oxygen atoms of O_3 (O1 and O3) simultaneously approach the C5 and C6 atoms. The forming C5–O1 and C6–O3

bonds reach lengths of 1.43 Å and 1.42 Å, respectively, while the original C5–C6 double bond is significantly elongated from 1.38 Å to 1.56 Å, indicating irreversible disruption of aromatic stabilization. This step represents the most favorable reaction pathway. Subsequently, the resulting unstable primary ozonide (POZ) intermediate IM6 undergoes concerted dissociation via transition state TS6-17. During this process, the O2–O3 bond elongates to 2.02 Å, and the C5–C6 bond extends to 1.96 Å, while new C5–O1 and C6–O3 bonds begin to form with lengths of approximately 1.32 Å and 1.26 Å, respectively. This leads to the formation of the vibrationally excited Criegee intermediate (CI) IM17, which is energetically the most favorable product.

The reaction of 2,4-DNP with •OH mainly proceeds through two competing mechanisms, namely ring addition and HAA, as shown in the blue region of Figure 2. In the electrophilic addition pathway, •OH preferentially attacks the C3 site, which is located between the two nitro groups and is meta to the hydroxyl substituent. This process proceeds through transition state TS3', where the distance between the oxygen atom of •OH and C3 decreases to 1.42 Å (from an initial separation of 1.99 Å). Concurrently, the C2–C3 and C3–C4 bond lengths increase from 1.40 Å to 1.50 Å, indicating significant disruption of the local aromatic structure and a redistribution of π-bonding within the ring. The O–H bond of •OH forms an angle of approximately 110° with the plane of the aromatic ring, a geometry that facilitates effective overlap between the p-orbital of •OH and the π-system of the benzene ring, thereby promoting σ-bond formation and ultimately yielding the hydroxycyclohexadienyl radical intermediate IM3'. In the HAA

pathway, •OH primarily captures the H atom directly bonded to the C5 site. This reaction proceeds through transition state TS9', in which the distance between the oxygen atom of •OH and the hydrogen on C5 shortens to 1.19 Å, the breaking C5–H bond elongates from 1.08 Å to 1.26 Å, and the O–H–C5 angle approaches 179°, which is characteristic of a hydrogen-abstraction transition state. This step produces the phenoxy radical intermediate IM9' and one molecule of H_2O. Notably, the OWDD analysis indicates that the carbon at C5 exhibits electrophilic character (low electron density). This is contrary to the conventional expectation for hydrogen abstraction by an electrophilic radical such as •OH. Nevertheless, the calculations show that this site remains the dominant abstraction site in the HAA pathway. This selectivity shift suggests that the HAA reaction of •OH may be governed by bond-strength control and transition-state electrostatic complementarity, rather than being determined solely by ground-state electrophile–nucleophile interactions. Indeed, the C–H bond dissociation energy has been established as a key factor controlling the site-selectivity of HAA by •OH, with weaker bonds being preferentially abstracted.

The green region in Figure 2 illustrates the reaction mechanism of $•NO_2$ with 2,4-DNP. Although the reaction pathways of 2,4-DNP with $•NO_2$ and •OH both involve two fundamental elementary steps, radical addition and HAA, significant differences exist in their reactivity and pathway selectivity. In the radical addition pathway, $•NO_2$ preferentially attacks the C3 site via transition state TS3*. During this process, the forming C3–O bond length gradually shortens, ultimately leading to the formation of the nitrocyclohexadienyl radical intermediate IM3*. This reaction mode resembles the

300 •OH-addition process suggesting some consistency in regioselectivity. However, HAA
301 pathway displays markedly different behavior. Unlike •OH, which mainly abstracts hy-
302 drogen atoms from the C5 site, •NO_2 preferentially abstracts the hydrogen atom of the
303 hydroxyl group through transition state TS7*. During this process, the breaking O–H
304 bond is significantly elongated from 0.98 Å to 1.21 Å, while the newly formed H–ONO
305 bond shortens from 1.08 Å to 0.97 Å.

306 This difference originates from the fundamentally different reaction characteristics
307 of the two radicals. The high reactivity of •OH allows it to overcome unfavorable
308 ground-state electrostatics and abstract the H atom at C5. By contrast, •NO_2 has much
309 weaker electrophilicity and lower reactivity; its hydrogen abstraction depends on elec-
310 trostatic complementarity and charge transfer, and it preferentially targets the hydroxyl
311 hydrogen(Shenghur et al., 2014). Moreover, the •NO_2-mediated hydrogen abstraction
312 is often accompanied by substantial charge transfer, with a mechanism that more
313 closely resembles proton-coupled electron transfer (PCET)(Tyburski et al., 2021). Thus,
314 the O–H bond is more readily cleaved than a C–H bond, making the hydroxyl hydrogen
315 the preferred abstraction site for •NO_2.

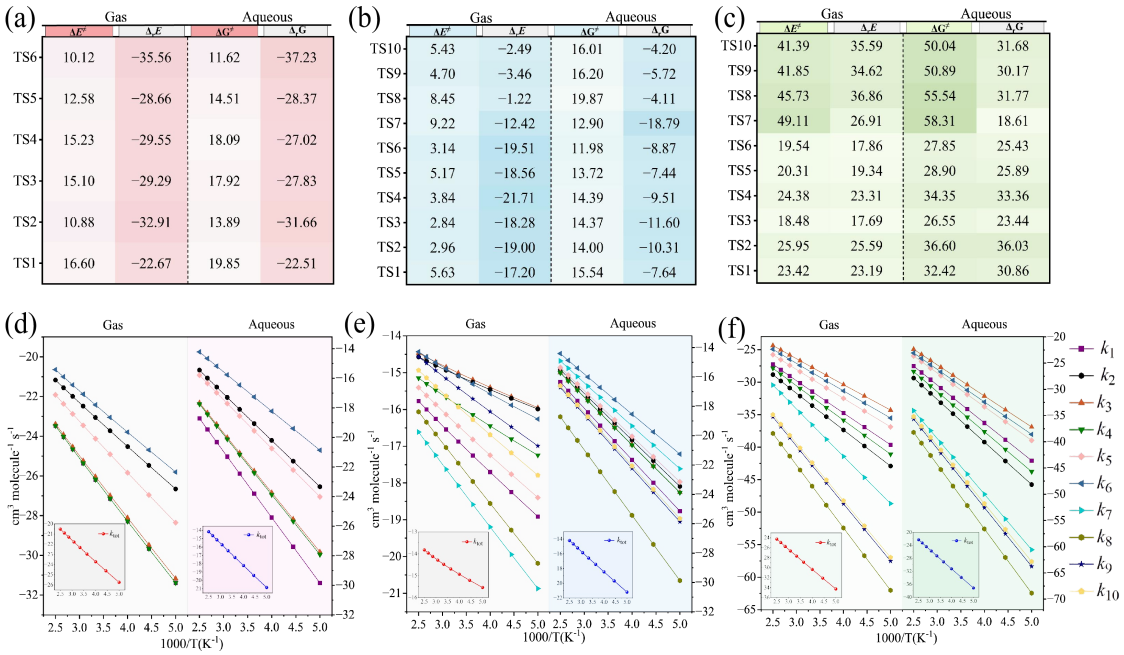


Figure 3 Thermodynamics, kinetics, and temperature dependence of the reactions of 2,4-DNP with O_3, •OH, and •NO_2. (a–c) reaction energy barriers ($\Delta E^{\neq}$) and reaction energies ($\Delta_r E$) for the key pathways (unit: kcal mol^{-1}). (d–e) Temperature-dependent reaction rate constants for the major channels.

The combined thermodynamic and kinetic analysis reveals that the reaction of O_3 with 2,4-DNP is both thermodynamically favorable and kinetically accessible in the gas and aqueous phases. As shown in Figure 3a, the most favorable gas-phase pathway, R6, has a low energy barrier of 10.12 kcal mol^{-1} and is strongly exothermic (ΔE = –35.56 kcal mol^{-1}). In the aqueous phase, although the barrier increases moderately to 11.62 kcal mol^{-1}, the reaction remains significantly exothermic. This indicates that solvation does not fundamentally alter the thermodynamic driving force, and the relatively low barrier ensures that the reaction remains kinetically feasible in both environmental media. In contrast, the reaction of 2,4-DNP with •OH shows even more favorable kinetics, consistent with its role as the major atmospheric oxidant. The addition pathway in the

gas phase proceeds with an exceptionally low barrier of 2.84 kcal mol^{-1}, substantially lower than the O_3- initiated pathway, as presented in Figure 3b. The HAA pathway also presents a low barrier of 4.70 kcal mol^{-1}. The similar barrier heights suggest that these two •OH-initiated pathways are kinetically competitive and are expected to occur concurrently under atmospheric conditions.

By comparison, the direct reaction of 2,4-DNP with $•NO_2$ is much less favorable. The overall process is endothermic and therefore non-spontaneous, as illustrated in Figure 3c. Among the two plausible direct reaction pathways, radical addition to the aromatic ring via the nitration pathway R3* has a calculated energy barrier of 18.48 kcal mol^{-1}, whereas HAA pathway has an even higher barrier of 41.39 kcal mol^{-1}, making it far less accessible. Although the nitration channel is kinetically favored over HAA in the $•NO_2$ system, its energy barrier is still great higher than those of the corresponding •OH-initiated pathways and is also less thermodynamically favorable than both •OH- and O_3-mediated reactions. Given these pronounced kinetic limitations, combined with the typically lower atmospheric concentration of $•NO_2$ relative to •OH and O_3, the calculations strongly suggest that the direct transformation of 2,4-DNP initiated by $•NO_2$ is negligible under ambient atmospheric conditions(Shi et al., 2025; Chapleski et al., 2016). Therefore, the atmospheric degradation of 2,4-DNP is expected to be dominated by oxidation processes initiated by •OH radicals and O_3. The possible involvement of $•NO_2$ in subsequent reactions with primary oxidation intermediates will be discussed separately to provide a complete mechanistic picture of its environmental fate.

This study further shows that the reaction behavior of 2,4-DNP in the aqueous phase differs markedly from that in gas phase and from that of simpler nitrophenol analogues. This difference is fundamentally attributed to the restructuring of molecular electronic distribution and reaction coordinates by the dynamic hydrogen-bonding network established between water and 2,4-DNP(Lyu et al., 2025). In contrast to the common trend in which solvation stabilizes polar transition states and thus lowers energy barriers in mononitrophenols, 2,4-DNP exhibits the distinctive features of increased aqueous-phase energy barriers and solvent-induced switching of regioselectivity.

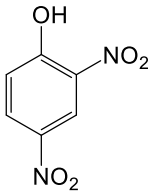
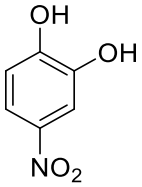
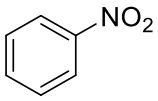
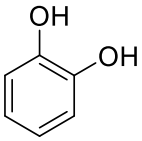
The increase in the aqueous-phase energy barriers can be attributed to the disruptive effect of the solvent on the intramolecular cooperativity inherent to 2,4-DNP. The simultaneous presence of a strongly electron-donating hydroxyl group and strongly electron-withdrawing nitro groups induces a pronounced intramolecular electric field, while the ortho-substitution geometry further enables stabilizing intramolecular hydrogen bonds(Albinet et al., 2010). These structural features provide significant ground-state stabilization in the gas phase. In aqueous solution, water molecules compete with the internal hydrogen-bonding pattern by interacting with the polar functional groups, thereby partially disrupting the intramolecular hydrogen-bond network and weakening the internal electric field, which raises the ground-state energy(Yang et al., 2023a). Solvent reorganization also imposes an energetic penalty. Although solvation stabilizes the transition state, the net effect is an increase in the overall reaction barrier. The change in site selectivity likewise arises from solvent-mediated electron redistribution and

pathway switching. In the ring-addition pathway of •OH, the C3 position is more favorable in the gas phase because of the dominant conjugation effects. In the aqueous phase, however, water molecules enhance the local polarization near the hydroxyl-adjacent carbon C6, making another site more competitive for attack. For hydrogen abstraction reactions, the gas-phase pathway is primarily governed by s bond dissociation strength, where the C5–H bond is weakened by the adjacent nitro group and is therefore more susceptible to homolysis. In the aqueous phase, the mechanism shifts toward a PCET-like process. The hydroxyl hydrogen, due to its intrinsic acidity and the proton-transfer assistance provided by the hydrogen-bonding network of water, gains both kinetic and thermodynamic advantages, becoming the dominant abstraction site in solution.

Kinetic calculations further quantify the feasibility differences among various pathways under atmospheric conditions. To ensure physical significance and environmental interpretability, all rate constants were converted into the standard unit commonly used in atmospheric chemistry (cm^3 $molecule^{-1}$ s^{-1}). Aqueous-phase data were converted from their original units of M^{-1} s^{-1} using the Avogadro constant and volume-unit conversion (1 M^{-1} s^{-1}= (1000/NA) cm^3 $molecule^{-1}$ s^{-1}≈ 1.66 × 10^{-21} cm^3 $molecule^{-1}$ s^{-1}). As shown in Figure 3d–e, the rate constants of all major channels increase with temperature over the range of 200–400 K, exhibiting a characteristic Arrhenius-type temperature dependence. The total rate constants of the dominant pathways are listed in Table S2. Specifically, the •OH pathway shows the highest kinetic activity, with total gas-phase and aqueous-phase rate constants of 3.18 × 10^{-15} cm^3 $molecule^{-1}$ s^{-}

[1] and 2.25×10^{-17} cm^3 $molecule^{-1}$ s^{-1}, respectively, at 298.15 K, further confirming its role as the dominant atmospheric oxidant. The O_3 pathway also shows notable activity in the aqueous phase, with a total aqueous-phase rate constant of 3.08×10^{-17} cm^3 $molecule^{-1}$ s^{-1}, highlighting the importance of aqueous environments in multiphase chemistry. In contrast, the direct $\bullet NO_2$ pathway exhibits extremely low kinetic activity, with total gas-phase and aqueous-phase rate constants as low as 1.75×10^{-28} cm^3 $molecule^{-1}$ s^{-1} and 3.93×10^{-28} cm^3 $molecule^{-1}$ s^{-1}, respectively. These values are more than 13 orders of magnitude lower than those of the •OH pathway. Even under conditions of elevated $\bullet NO_2$ concentration, the contribution of this pathway to the transformation of 2,4-DNP is expected to be negligible. In summary, the atmospheric degradation of 2,4-DNP is kinetically dominated by •OH, with O_3 playing a significant role in the aqueous phase, while the direct transformation contribution of $\bullet NO_2$ can be neglected in environmental assessments.

Table 1 The experimental rate constant (cm^3 $molecule^{-1}$ s^{-1}) values of various phenols with O_3 in the gas phase.

Compound	Structure formula	Rate constants (cm^3 $molecule^{-1}$ s^{-1})
2,4-DNP		4.23×10^{-23}
4-Nitrocatechol		1.48×10^{-20}(Wang et al., 2026)
Nitrobenzene		$(7.00 \pm 0.20) \times 10^{-21}$(Atkinson et al., 1987)
Catechol		$(9.60 \pm 1.12) \times 10^{-18}$(Sun et al., 2022; Tomas et al., 2003)

This study establishes the reliability of the theoretically derived rate constant for the reaction between 2,4-DNP and ozone through systematic benchmarking against available experimental and computational data for structurally related aromatic compounds. Although direct experimental measurements for this specific reaction are currently unavailable, as summarized in Table 1, the theoretical rate constant for the mononitro analogue nitrocatechol (1.48×10^{-20} cm^3 $molecule^{-1}$ s^{-1})(Wang et al., 2026) is approximately three orders of magnitude lower than that of catechol(Sun et al., 2022; Tomas et al., 2003), clearly demonstrating the strong inhibitory effect of the nitro group, as an electron-withdrawing functional group on the ozone reactivity of the aromatic ring. Building on this trend, the calculated rate constant for the dinitro compound 2,4-

DNP (4.23×10^{-23} cm^3 $molecule^{-1}$ s^{-1}) is reduced by an additional three orders of magnitude, quantitatively reflecting the cumulative electron-withdrawing effect of the two nitro substituents. This result is consistent with established activity trends of nitro-substituted aromatic systems, thereby supporting the reasonableness of the calculated rate constant.

Furthermore, the predominance of substituent electronic effects in governing reactivity is independently corroborated. As detailed in Table S3, a systematic comparison of the theoretical rate constants for the reaction of 2,4-DNP with •OH with data for structural analogues demonstrates that the strong electron-withdrawing character of the nitro groups likewise controls the kinetics of this pathway. This consistency suggests that the electronic influence of nitro substituent is general across different oxidants rather than being restricted to a single mechanism. Collectively, these results establish a robust and quantitatively consistent framework for predicting the atmospheric oxidation kinetics of aromatic pollutants on the basis of their fundamental electronic structure.

3.1.3 The subsequent reactivity mechanism of the key intermediate IM3'

As the primary initiator of atmospheric degradation of 2,4-DNP, •OH generates the key radical intermediate IM3' via electrophilic addition. This highly reactive species can rapidly undergo secondary reactions with surrounding atmospheric constituents. Reaction with molecular O_2 typically governs its rapid oxidative evolution, while reaction with $•NO_2$ can lead to the formation of more toxic and more strongly light-absorbing nitrated products. Therefore, to fully delineate the atmospheric transformation

pathways and final products of 2,4-DNP, it is essential to systematically investigate the reaction mechanisms of IM3' with O_2 as well as $\bullet NO_2$.

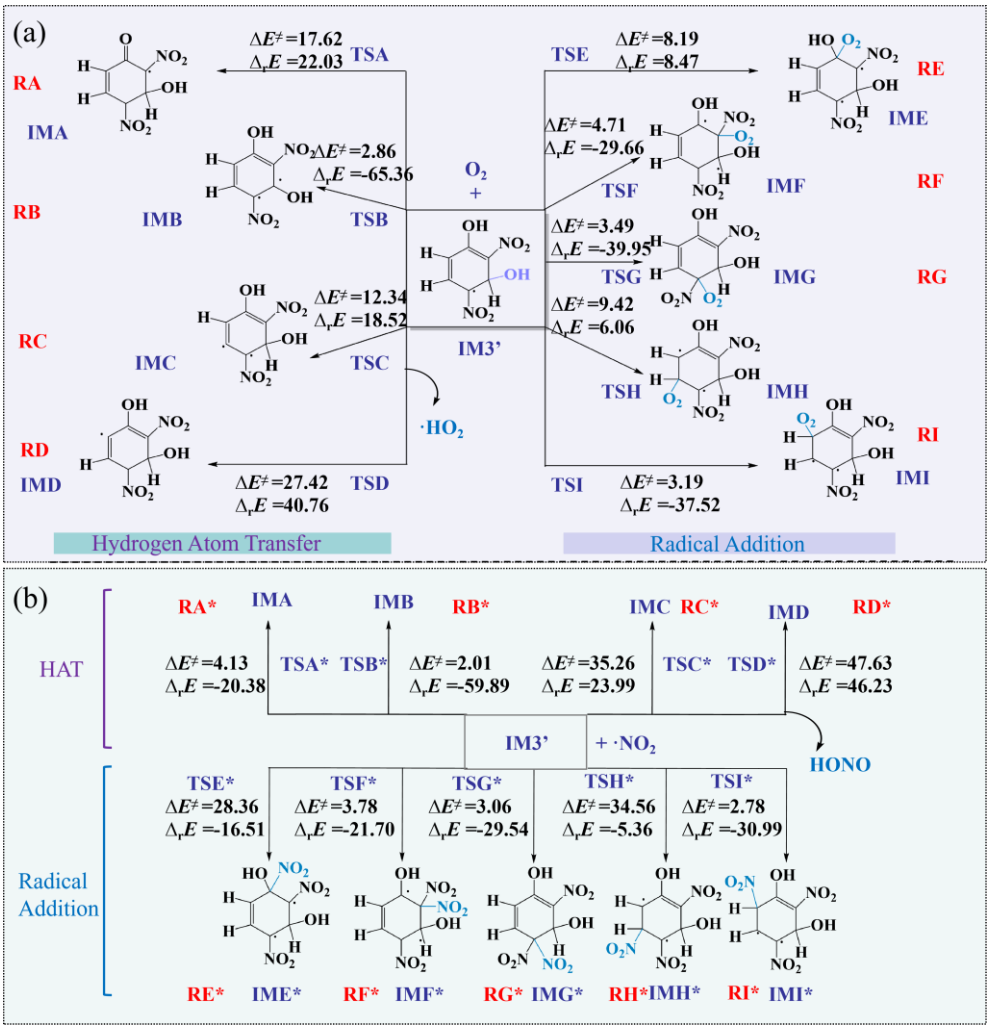


Figure 4 The subsequent reactivity mechanism of the key intermediate IM3' (unit: kcal mol^{-1}).

A systematic analysis was conducted for the reaction pathways of the intermediate IM3' with O_2 and $\bullet NO_2$. For the reaction with O_2, as shown in Figure 4a, IM3' prime mainly evolves through two competing pathways, namely HAA and radical addition. The HAA pathway contains four distinct subchannels, among which the RB channel is the most favorable both thermodynamics and kinetics. It is characterized by a remark-

ably low transition-state energy barrier of 2.86 kcal mol^{-1} and a highly exothermic reaction energy of –65.36 kcal mol^{-1}. In this process, the O_2 molecule approaches the activated C3–H bond. The reaction is directed to the C3 position because this carbon is flanked by two strongly electron-withdrawing nitro groups at the adjacent C2 and C4 positions. This electronic effect substantially lowers the electron density and weakens the C3–H bond, making it the most favorable site for hydrogen abstraction. Key structural parameters in transition state TSB reveal a concerted mechanism: the distance between the attacking oxygen atom Oa of O_2 and the transferring hydrogen shortens to approximately 1.17 Å, while the breaking C3–H bond elongates to about 1.30 Å. This synchronous bond-breaking and bond-forming process yields the phenoxy radical intermediate IMB and the hydroperoxyl radical ($•HO_2$). In contrast, the other HAA channels involving abstraction from the C5, C6, or hydroxyl positions have much higher energy barriers and are therefore kinetically uncompetitive under realistic atmospheric conditions. In the competing radical addition pathway, the most favorable channel is RI, in which O_2 adds to the relatively electron-rich C4 position via the transition state TSI. This process has an energy barrier of 3.19 kcal mol^{-1} and is exothermic by –37.52 kcal mol^{-1}. Because this barrier is close to that of the optimal HAA channel RB, the HAA and radical addition pathways for the reaction of IM3' with O_2 are expected to compete directly at the molecular level.

The reaction of IM3' with $•NO_2$ similarly follows a competitive mechanism involving HAA and radical addition (Figure 4b). Within the HAA pathway, the RB* channel shows a clear advantage analogous similar to that observed in the O_2 system,

with a low energy barrier of 2.01 kcal mol^{-1} and a highly exothermic reaction energy of –59.89 kcal mol^{-1}. The mechanism of this process is highly consistent with that of the O_2-involved RB channel, which both involve the oxidant abstracting the hydrogen atom from the C3 position, yielding the identical phenoxy radical intermediate IMB, while producing HONO or •HO_2, respectively. In the radical addition pathway, the most feasible route is the channel RI*, with a barrier of 2.78 kcal mol^{-1} and a reaction energy of –30.99 kcal mol^{-1}. Similar to the O_2 addition pathway, •NO_2 preferentially adds to the relatively electron-dense C4 position, generating the nitro-substituted cyclohexadienyl radical intermediate IMI*. Comparison of the lowest energy barriers for the two pathways reveals that the HAA path is kinetically and slightly more favorable than the radical addition path. This establishes the HAA mechanism as the dominant mechanism in the reaction of IM3' with •NO_2, consistent with the conclusion drawn for the O_2 system.

The above computational results elucidate, at the microscopic mechanistic level, the possible pathways of IM3' with O_2 and •NO_2. However, to assess its ultimate fate in the real atmospheric, it is necessary to further consider the competition between these oxidants under realistic atmospheric concentrations. In particular, the large concentration difference between O_2 and •NO_2 must be taken into account when evaluating the dominant degradation channels and their environmental significance.

3.2. Molecular dynamics

Although the homogeneous oxidation mechanisms of 2,4-DNP in the gas and aqueous phases have been clarified, its heterogeneous interfacial behavior on aerosol particle surfaces remains to be elucidated. As a representative model of atmospheric

nanoparticles, C60 offers an ideal system for probing the non-covalent interactions between pollutants and particulate matter, owing to its well-defined carbon framework and surface curvature(Athar and Patnaik, 2022). In this study, the IGM was employed to qualitatively and quantitatively analyze the weak interactions within the adsorption complexes(Lu and Chen, 2022), thereby revealing the interactions that govern the interfacial behavior at the molecular level.

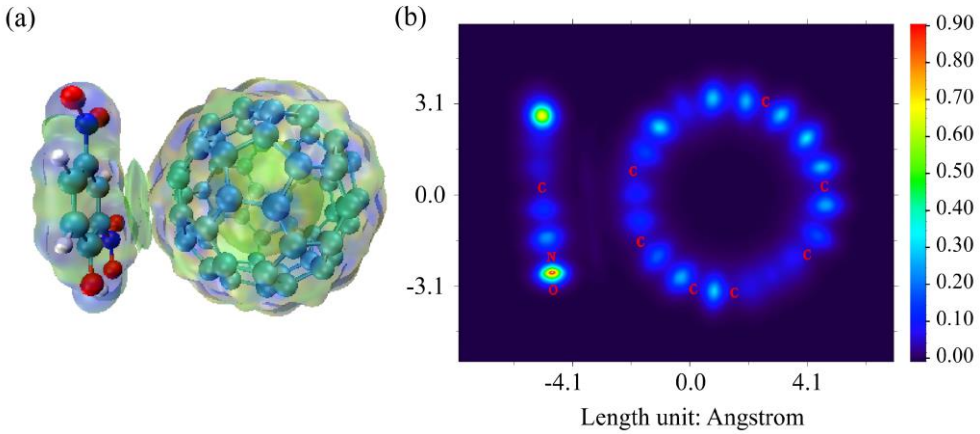


Figure 5 IGM analysis of intermolecular interactions in the 2,4-DNP-C60 aggregate. (a) three-dimensional (3D) IGM isosurface map. (b) Two-dimensional (2D) IGM density map.

The intermolecular interactions within the 2,4-DNP-C60 aggregate were characterized utilizing the Independent Gradient Model by defining each monomer as an individual fragment. The intermolecular interaction pattern at the 2,4-DNP-C60 interface is elucidated jointly by the three-dimensional IGM isosurface map (Figure 5a) and the two-dimensional density map (Figure 5b), which exhibit excellent consistency. According to the principles of IGM analysis, the green and light-green isosurface regions,

where sign(λ2) ≈ 0, correspond to van der Waals (vdW) interactions, indicative of diffuse and non-directional weak attractions. In contrast, the blue regions, characterized by sign(λ2) < 0, indicate directional interactions such as hydrogen bonds or strong electrostatic attractions, which are associated with more localized electron-density distributions.

Specifically, the extensive green/light-green isosurface between the C60 cage and the benzene ring of 2,4-DNP corresponds closely to the continuous blue-to-light-blue signal band in the 2D density map (δg_{inter} ≈ 0.10–0.30), confirming that vdW interactions, mainly dispersion and induction forces arising from the π-electron clouds of the benzene ring and fullerene surface, dominant the interfacial binding between 2,4-DNP and C60. Meanwhile, distinct blue regions are observed near the polar functional groups of 2,4-DNP, namely the nitro and hydroxyl moieties. These features manifest as localized yellow-green hotspots in the 2D density map (δg_{inter} ≈ 0.60–0.80), eindicating stronger polar interactions. These interactions can be attributed to specific directional forces, including a C–H···π hydrogen bond involving the hydrogen atom of the –OH group and the delocalized π-electron cloud of C60, as well as a dipole-π interaction between the oxygen atoms of the $–NO_2$ groups and the fullerene surface. These synergistic polar interactions enhance both the binding selectivity and the overall stability of the 2,4-DNP-C60 interface.

Further analysis indicates that the 2,4-DNP molecule preferentially adsorbs with its benzene ring approximately parallel to the C60 surface. In this configuration, the

nonpolar benzene ring maximizes the dispersion interaction area by closely approaching the carbon cage via vdW forces, while the polar –OH and $–NO_2$ groups remain oriented outward. This arrangement not only avoids steric repulsion with the C60 surface corresponding to strong steric hindrance, but also facilitates hydrogen-bond-network formation between the polar groups of neighboring 2,4-DNP molecules. In the 2D IGM cross-sectional map, this orientation is reflected by a clear spatial separation between the polar hotspots of the 2,4-DNP and the van der Waals signal band associated with C60, with the hotspot positions precisely corresponding to the atomic coordinates of the polar functional groups.

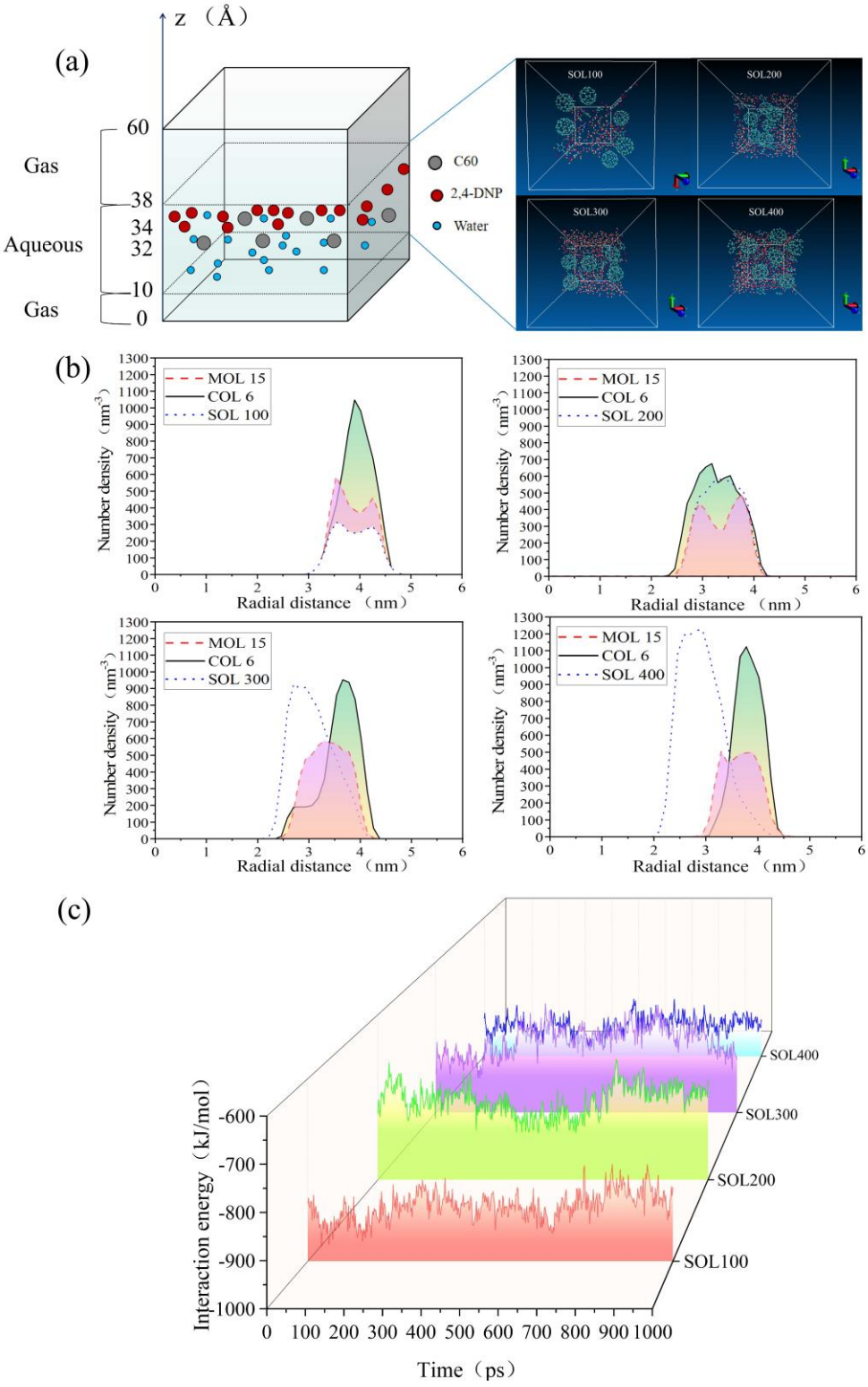


Figure 6 (a) Molecular dynamics simulation framework construction (MOL: 2,4-DNP; COL: C60; SOL: water). (b) z-axis number density profile of molecules (units: nm^{-3}). (c) Hydration-dependent adsorption energies of 2,4-DNP on C60 (units: kJ mol^{-1}).

Building upon the fundamental interaction mechanisms revealed by IGM in the anhydrous system, molecular dynamics simulations were further carried out to how hydration, as a key environmental factor, dynamically regulates the adsorption behavior of 2,4-DNP on C60 under atmospherically relevant conditions. Figure 6a illustrates the initial simulation setup, which consists of 15 molecules of 2,4-DNP and 6 molecules of C60 placed in a three-layer simulation box measuring 30 × 30 × 60 $Å^3$, with a gas-aqueous-gas sandwich structure. Different hydration levels were modeled by varying the number of water molecules from SOL100 to SOL400. The system then underwent energy minimization and molecular dynamics relaxation to obtain an equilibrated structure. In the aqueous phase, the distribution of 2,4-DNP and C60 gradually shifted toward the center of the water layer as the number of water molecules increased, indicating that the introduction of water significantly altered the spatial distribution pattern of the solutes.

The number-density distribution profiles along the z-axis in Figure 6b further reveal the influence of hydration on the axial distribution and aggregation behavior of the solute molecules. Combined with the strong intermolecular interactions revealed by IGM in the anhydrous system, it can be inferred that under low hydration conditions, 2,4-DNP and C60 tend to form compact aggregates because of their relatively strong mutual attraction. As the number of water molecules increases from SOL200 to SOL400, the density peak shifts toward larger radial distances (4.0–4.5 nm) and its height gradually rises. This indicates that water molecules disrupt the close aggregation tendency between 2,4-DNP and C60 through steric hindrance effects, promoting the

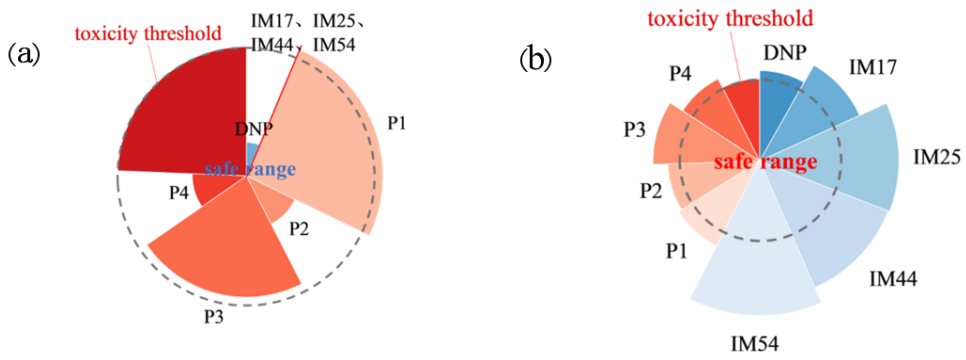
outward diffusion of solute molecules along the z-axis and thereby significantly enhancing the overall dispersity of the system.

Based on the temporal evolution of the interaction energies shown in Figure 6c, the dynamic regulatory role of hydration on intermolecular adsorption behavior can be further interpreted from an energetic perspective. In the low-hydration system SOL100, the interaction energy remains stable at approximately –850 kJ mol^{-1}. Its relatively large negative value is consistent with the compact aggregated state shown in Figure 6b, indicating strong direct adsorption between 2,4-DNP and C60 under these conditions. As the number of water molecules increases to SOL200, the absolute value of the interaction energy increases further, suggesting enhanced intermolecular attraction. This change may originate from moderate hydration, where water molecules promote specific orientations and stabilize solute interactions through effects such as dielectric screening or indirect bridging(Lyu et al., 2025). However, when the hydration level further increases to SOL400, the absolute value of the interaction energy decreases, implying a significant weakening of intermolecular adsorption. This indicates that under high hydration conditions, water molecules suppress the direct interaction between 2,4-DNP and C60, thereby driving the system toward a more dispersed and stable solvated state. This non-monotonic energy trend, which first strengthens and then weakens, is consistent with the morphological evolution of solute distribution shown in Figure 6b, namely a transition from an initially aggregated state to a more dispersed one. Together, these results reveal the complex regulatory role of hydration in interfacial adsorption behavior.

To assess statistical uncertainty arising from initial conditions, four independent replica simulations were performed for each hydration level by assigning distinct initial atomic velocities, thereby generating statistically independent trajectories in phase space. Error analysis demonstrates that the main conclusions regarding the adsorption configuration and distribution of 2,4-DNP at the gas-aqueous interface remain consistent across all replicas, underscoring the robustness and reproducibility of the results.

3.3 Ecotoxicity assessment

The reaction of ozone with aromatic rings follows a relatively well-defined mechanism and produces a comparatively clear product spectrum, making it a comparatively model for evaluating the directional impact of atmospheric oxidation on the toxicity of 2,4-DNP. By focusing on O_3, the oxidant with of high environmental relevance, this study enables a precise analysis of the oxidation degradation pathways of 2,4-DNP and the toxicity of its products. The conclusions drawn here can provide a crucial toxicological reference for future investigations of the more complex atmospheric oxidation networks involving radicals such as •OH and •NO_2. Accordingly, based on the key intermediates and final products (IM17, IM25, IM44, IM54, P1–P4) identified in Figure S2, their mutagenic and developmental toxicity potentials were predicted using the T.E.S.T. tool(Epa, 2020), aiming to reveal the toxicity evolution pattern along this specific oxidation process.



Ames Mutagenicity Developmental Toxicity Potential

Figure 7 Toxicity prediction of 2,4-DNP and its transformation products. (a) Ames mutagenicity. (b) Developmental toxicity.

The risk differences in Ames mutagenicity and developmental toxicity potential between 2,4-DNP and the intermediates (IMs series) and final products (Ps series) generated from its reaction with ozone are intuitively illustrated in Figure 7. Regarding Ames mutagenicity in Figure 7a, the parent compound 2,4-DNP exhibits a predicted value of 0.13 that falls within the safety threshold. The specific data are presented in Table S4. In contrast, its ozonolysis products display a marked divergence in mutagenic potential. Although primary intermediates (IM17, IM25, IM44, IM54) show no detectable mutagenicity, the final products generally demonstrate elevated mutagenic risk. Notably, the predicted value for product P1 (0.53) exceeds the toxicity threshold, placing it within the high-risk zone. This result clearly indicates that the ozonolysis does not necessarily reduce the mutagenicity of 2,4-DNP, instead, by generating more reactive intermediates and final products, it may significantly increase the overall genotoxic risk of the reaction system.

In terms of developmental toxicity in Figure 7b, 2,4-DNP itself shows a baseline potential of 0.55, which is further exacerbated by ozonolysis. All derived products show

higher developmental toxicity than the parent compound, with the risk reaching a maximum for IM54 (0.94). Notably, P2 and P4, despite their relatively low Ames mutagenicity (0.21), still exhibit a developmental toxicity potential of 0.56, which are higher than that of the parent compound. This reveals a decoupling between mutagenicity and developmental toxicity, suggesting that the oxidation process may generate novel hazardous specific developmental toxicity even when their mutagenic potential remains relatively low. Overall, the analysis indicates that the ozonolysis of 2,4-DNP does not constitute a harmless degradation pathway. On the contrary, it leads to the generation of more intermediate and final products with enhanced mutagenic and developmental toxicity.

The QSAR models utilized in this study provide valuable preliminary information for risk prioritization, the inherent uncertainties associated with in silico predictions must be acknowledged. The predictive performance is fundamentally constrained by the chemical space of the training sets and the defined applicability domains. For structurally distinct species such as 2,4-DNP and its various derivatives, the confidence levels of the predictions may be diminished because these models cannot fully elucidate specific toxicological modes of action. In addition, categorical predictions with probability scores close to threshold are inherently unstable, suggesting that the "not detected" Ames mutagenicity signals for intermediates such as IM17, IM25, IM44, and IM54 may reflect model limitations rather than a definitive absence of toxicity. These compounds should therefore be regarded as high-priority targets for experimental validation. Furthermore, these computational frameworks necessarily simplify complex biological

endpoints such as developmental toxicity. Therefore, the present findings should be interpreted as hypothesis-generating rather than definitive. Future studies are recommended to validate these predictions through in vitro Ames tests and zebrafish embryo development experiments, and to develop targeted removal strategies for toxic nitrocarbonyl-type products.

4 Conclusion

This study systematically investigated the chemical transformation mechanisms, multiphase interfacial behavior, and toxicity evolution of 2,4-DNP in the atmosphere using an integrated computational framework combining DFT, MD simulations, and QSAR models. The main quantitative findings are: the atmospheric degradation of 2,4-DNP is dominated by •OH and O_3 oxidation pathways, while direct reaction with •NO_2 is kinetically unfavorable (gas-phase rate constant ~10^{-28} cm^3 $molecule^{-1}$ s^{-1}, more than 13 orders of magnitude lower than that of •OH); solvation effects and the electron-withdrawing nitro groups suppress the initial reaction rates; the key radical intermediate from •OH addition reacts with O_2 and •NO_2 predominantly via HAA; MD simulations reveal that the adsorption behavior of 2,4-DNP on atmospheric particle surrogates is regulated non-monotonically by the degree of interfacial hydration. Under low-hydration conditions, solute-particle interactions are enhanced, while under high-hydration conditions, adsorption is weakened due to competitive binding and steric hindrance effects from water molecules; and ozonolysis of 2,4-DNP does not lead to harmless degradation but generates secondary products with significantly increased mutagenicity and developmental toxicity. Collectively, 2,4-DNP is a relatively persistent pollutant

whose atmospheric lifetime depends strongly on humidity and whose oxidation does not detoxify but rather amplifies environmental risk. Compared to previous studies that focused on gas-phase photolysis and assumed oxidative detoxification, our work quantifies the cumulative electron-withdrawing effect of two nitro groups (rate constant three orders lower than mononitrocatechol) and reveals that ozonolysis increases toxicity, challenging conventional assumptions.

Several limitations should be noted: the aerosol surrogate (C60) and QSAR toxicity models do not fully capture real atmospheric particle complexity or definitive toxicological outcomes; experimental validation via in vitro and in vivo assays is needed. Despite these caveats, our findings have clear implications for atmospheric chemistry and climate. The humidity-dependent adsorption behavior implies that 2,4-DNP may have longer residence time and greater long-range transport under dry conditions, affecting its global distribution. Moreover, the production of toxic transformation products suggests that current air quality models may underestimate the health risks of nitrophenolic emissions. Regulatory attention to 2,4-DNP and its derivatives is therefore warranted.

Data availability

The data supporting this article have been included as part of the supplementary information or are available upon request.

Author contributions

Chenlei Wang conceptualized the study, curated the data, validated the results, and wrote the original draft. Ran Li and Jiaxing Sun conceptualized the study and curated

the data. Zihan Zhang curated the data. Nan Zhao developed the software and validated the results. Zuju Ma developed the software, performed the visualization, and carried out the investigation. Maoxia He developed the methodology, performed the visualization, and carried out the investigation. Leilei Liu reviewed and edited the manuscript and acquired the funding. Jianfei Sun curated the data, reviewed and edited the manuscript, acquired the funding, supervised the project, and administered the project.

Competing interests

The authors declare that they have no conflict of interest.

Acknowledgements

This work was financially supported by Shandong Provincial Natural Science Foundation ZR2024MB037, and Natural Science Foundation of Yantai 2024JCYJ065.

References

Ahmaruzzaman, M., Mishra, S. R., Gadore, V., Yadav, G., Roy, S., Bhattacharjee, B., Bhuyan, A., Hazarika, B., Darabdhara, J., and Kumari, K.: Phenolic compounds in water: From toxicity and source to sustainable solutions - An integrated review of removal methods, advanced technologies, cost analysis, and future prospects, Journal of Environmental Chemical Engineering, 12, 10.1016/j.jece.2024.112964, 2024.

Albinet, A., Minero, C., and Vione, D.: Phototransformation processes of 2,4-dinitrophenol, relevant to atmospheric water droplets, Chemosphere, 80, 753-758, 10.1016/j.chemosphere.2010.05.016, 2010.

Athar, M. and Patnaik, A.: Through-Bond-Driven Through-Space Interactions in a Fullerene C60 Noncovalent Dyad: An Unusual Strong Binding between Spherical and Planar π Electron Clouds and Culmination of Dyadic Fractals, Journal of Physical Chemistry A, 126, 3629-3641, 10.1021/acs.jpca.1c10828, 2022.

Atkinson, R., Tuazon, E. C., Wallington, T. J., Aschmann, S. M., Arey, J., Winer, A. M., and Pitts, J. N.: Atmospheric chemistry of aniline, N,N-dimethylaniline, pyridine, 1,3,5-

triazine, and nitrobenzene, Environmental Science & Technology, 21, 64-72, 10.1021/es00155a007, 1987.

Barton, D. H. R. and Cookson, R. C.: The Principles of Conformational Analysis, Quarterly Reviews, 10, 44-82, 10.1039/qr9561000044, 1956.

Benfenati, E., Benigni, R., DeMarini, D. M., Helma, C., Kirkland, D., Martin, T. M., Mazzatorta, P., Ouédraogo-Arras, G., Richard, A. M., Schilter, B., Schoonen, W., Snyder, R., and Yang, C.: Predictive Models for Carcinogenicity and Mutagenicity: Frameworks, State-of-the-Art, and Perspectives, Journal of Environmental Science and Health Part C-Environmental Carcinogenesis & Ecotoxicology Reviews, 27, 57-90, 10.1080/10590500902885593, 2009.

Canneaux, S., Bohr, F., and Henon, E.: KiSThelP: A Program to Predict Thermodynamic Properties and Rate Constants from Quantum Chemistry Results, Journal of Computational Chemistry, 35, 82-93, 10.1002/jcc.23470, 2014.

Cassano, A., Manganaro, A., Martin, T., Young, D., Piclin, N., Pintore, M., Bigoni, D., and Benfenati, E.: CAESAR models for developmental toxicity, Chemistry Central Journal, 4, 10.1186/1752-153x-4-s1-s4, 2010.

Chapleski, R. C., Zhang, Y. F., Troya, D., and Morris, J. R.: Heterogeneous chemistry and reaction dynamics of the atmospheric oxidants, O_3, NO_3, and OH, on organic surfaces, Chemical Society Reviews, 45, 3731-3746, 10.1039/c5cs00375j, 2016.

Delaria, E. R. and Cohen, R. C.: Measurements of Atmosphere-Biosphere Exchange of Oxidized Nitrogen and Implications for the Chemistry of Atmospheric NOx, Accounts of Chemical Research, 56, 1720-1730, 10.1021/acs.accounts.3c00090, 2023.

EPA, U. S.: User's Guide for T.E.S.T. (version 5.1) (Toxicity Estimation Software Tool): A Program to Estimate Toxicity from Molecular Structure., U.S. Environmental Protection Agency, 2020.

Fan, W. L., Chen, T., Zhu, Z. L., Zhang, H., Qiu, Y. L., and Yin, D. Q.: A review of secondary organic aerosols formation focusing on organosulfates and organic nitrates, Journal of Hazardous Materials, 430, 10.1016/j.jhazmat.2022.128406, 2022.

Frisch, M. J., Trucks, G. W., Schlegel, H. B., Scuseria, G. E., Robb, M. A., Cheeseman, J. R., Scalmani, G., Barone, V., Petersson, G. A., Nakatsuji, H., Li, X., Caricato, M.,

Marenich, A. V., Bloino, J., Janesko, B. G., Gomperts, R., Mennucci, B., Hratchian, H. P., Ortiz, J. V., Izmaylov, A. F., Sonnenberg, J. L., Williams, Ding, F., Lipparini, F., Egidi, F., Goings, J., Peng, B., Petrone, A., Henderson, T., Ranasinghe, D., Zakrzewski, V. G., Gao, J., Rega, N., Zheng, G., Liang, W., Hada, M., Ehara, M., Toyota, K., Fukuda, R., Hasegawa, J., Ishida, M., Nakajima, T., Honda, Y., Kitao, O., Nakai, H., Vreven, T., Throssell, K., Montgomery Jr., J. A., Peralta, J. E., Ogliaro, F., Bearpark, M. J., Heyd, J. J., Brothers, E. N., Kudin, K. N., Staroverov, V. N., Keith, T. A., Kobayashi, R., Normand, J., Raghavachari, K., Rendell, A. P., Burant, J. C., Iyengar, S. S., Tomasi, J., Cossi, M., Millam, J. M., Klene, M., Adamo, C., Cammi, R., Ochterski, J. W., Martin, R. L., Morokuma, K., Farkas, O., Foresman, J. B., and Fox, D. J.: Gaussian 16 Rev. C.01, 2016.

Grundlingh, J., Dargan, P. I., El-Zanfaly, M., and Wood, D. M.: 2,4-dinitrophenol (DNP): a weight loss agent with significant acute toxicity and risk of death, J Med Toxicol, 7, 205-212, 10.1007/s13181-011-0162-6, 2011.

Hu, W., Liu, D. D., Su, S. H., Ren, L. J., Ren, H., Wei, L. F., Yue, S. Y., Xie, Q. R., Zhang, Z. M., Wang, Z. H., Yang, N., Wu, L. B., Deng, J. J., Qi, Y. L., and Fu, P. Q.: Photochemical Degradation of Organic Matter in the Atmosphere, Advanced Sustainable Systems, 5, 10.1002/adsu.202100027, 2021.

Humphrey, W., Dalke, A., and Schulten, K.: VMD: Visual molecular dynamics, Journal of Molecular Graphics, 14, 33-38, https://doi.org/10.1016/0263-7855(96)00018-5, 1996.

Kroll, J. H. and Seinfeld, J. H.: Chemistry of secondary organic aerosol: Formation and evolution of low-volatility organics in the atmosphere, Atmospheric Environment, 42, 3593-3624, 10.1016/j.atmosenv.2008.01.003, 2008.

Kromann, J. C., Steinmann, C., and Jensen, J. H.: Improving solvation energy predictions using the SMD solvation method and semiempirical electronic structure methods, Journal of Chemical Physics, 149, 10.1063/1.5047273, 2018.

Lee, D., Schwegler, E., and Kanai, Y.: Dependence of Water Dynamics on Molecular Adsorbates near Hydrophobic Surfaces: First-Principles Molecular Dynamics Study, Journal of Physical Chemistry C, 118, 8508-8513, 10.1021/jp502850k, 2014.

Lefebvre, C., Rubez, G., Khartabil, H., Boisson, J. C., Contreras-García, J., and Hénon, E.: Accurately extracting the signature of intermolecular interactions present in the NCI plot of the reduced density gradient versus electron density, Physical Chemistry Chemical Physics, 19, 17928-17936, 10.1039/c7cp02110k, 2017.

Li, J., Han, Z. W., Sun, Y. L., Li, J. W., and Liang, L.: Chemical formation pathways of secondary organic aerosols in the Beijing-Tianjin-Hebei region in wintertime, Atmospheric Environment, 244, 10.1016/j.atmosenv.2020.117996, 2021.

Li, J., Han, Z. W., Wu, J., Tao, J., Li, J. W., Sun, Y. L., Liang, L., Liang, M. J., and Wang, Q. G.: Secondary organic aerosol formation and source contributions over east China in summertime, Environmental Pollution, 306, 10.1016/j.envpol.2022.119383, 2022a.

Li, M., Wang, X. F., Lu, C. Y., Li, R., Zhang, J., Dong, S. W., Yang, L. X., Xue, L. K., Chen, J. M., and Wang, W. X.: Nitrated phenols and the phenolic precursors in the atmosphere in urban Jinan, China, Science of the Total Environment, 714, 10.1016/j.scitotenv.2020.136760, 2020.

Li, M., Wang, X. F., Zhao, Y. N., Du, P., Li, H. Y., Li, J. R., Shen, H. Q., Liu, Z. Y., Jiang, Y. R., Chen, J., Bi, Y. J., Zhao, Y., Xue, L. K., Wang, Y., Chen, J. M., and Wang, W. X.: Atmospheric Nitrated Phenolic Compounds in Particle, Gaseous, and Aqueous Phases During Cloud Events at a Mountain Site in North China: Distribution Characteristics and Aqueous-Phase Formation, Journal of Geophysical Research-Atmospheres, 127, 10.1029/2022jd037130, 2022b.

Li, P. Y., Feng, L., Li, G. Y., and Bai, F. Q.: Effects of Electron Donating Ability of Substituents and Molecular Conjugation on the Electronic Structures of Organic Radicals, Chemical Research in Chinese Universities, 39, 202-207, 10.1007/s40242-023-2364-2, 2023.

Liu, X. H., Meng, T. T., Bai, F. Y., Ni, S., and Zhao, Z.: Theoretical investigation on the atmospheric degradation mechanism, kinetics, and fate of hydroxymethyl nitrate initiated by OH radicals, New Journal of Chemistry, 47, 11414-11424, 10.1039/d3nj01628e, 2023.

Liu, Z. Y. and Lu, T.: Theoretical Insight into Complexation Between Cyclocarbons and C60 Fullerene, Chemistry-a European Journal, 30, 10.1002/chem.202402227, 2024.

Lu, T., TST calculator, http://sobereva.com/310 (accessed 12 11, 2025).

Lu, T., Sobtop, Version [1.0], http://sobereva.com/soft/Sobtop (accessed on 17 01 2026).

Lu, T. and Chen, F. W.: Multiwfn: A multifunctional wavefunction analyzer, Journal of Computational Chemistry, 33, 580-592, 10.1002/jcc.22885, 2012.

Lu, T. and Chen, Q. X.: Independent gradient model based on Hirshfeld partition: A new method for visual study of interactions in chemical systems, Journal of Computational Chemistry, 43, 539-555, 10.1002/jcc.26812, 2022.

Lyu, Y., Xu, H., Yuan, H. X., Cui, Y. L., Zhang, C. Z., and Meng, Q. T.: Intermolecular interaction mechanisms between dinitrophenol and water: a molecular dynamics and DFT study, European Physical Journal Plus, 140, 10.1140/epjp/s13360-025-06478-8, 2025.

Maeda, S., Harabuchi, Y., Ono, Y., Taketsugu, T., and Morokuma, K.: Intrinsic Reaction Coordinate: Calculation, Bifurcation, and Automated Search, International Journal of Quantum Chemistry, 115, 258-269, 10.1002/qua.24757, 2015.

Mahilang, M., Deb, M. K., and Pervez, S.: Biogenic secondary organic aerosols: A review on formation mechanism, analytical challenges and environmental impacts, Chemosphere, 262, 10.1016/j.chemosphere.2020.127771, 2021.

Mangotra, A. and Singh, S. K.: Volatile organic compounds: A threat to the environment and health hazards to living organisms - A review, Journal of Biotechnology, 382, 51-69, 10.1016/j.jbiotec.2023.12.013, 2024.

Mao, Y. F., Qin, H., Huang, W. X., Lei, Y. S., Gao, X. J., Zhou, T. H., Wu, D. L., and Xu, L. Q.: Toward an atomic-scale understanding of competitive adsorption between ions and molecules near aqueous interfaces, Chemical Engineering Journal, 495, 10.1016/j.cej.2024.153699, 2024.

McNeill, V. F.: Atmospheric Aerosols: Clouds, Chemistry, and Climate, Annual Review of Chemical and Biomolecular Engineering, 8, 10.1146/annurev-chembioeng-060816-101538, 2017.

Nagy, P. R.: State-of-the-art local correlation methods enable affordable gold standard quantum chemistry for up to hundreds of atoms, Chem Sci, 15, 14556-14584, 10.1039/d4sc04755a, 2024.

Ohto, T., Dodia, M., Imoto, S., and Nagata, Y.: Structure and Dynamics of Water at the Water-Air Interface Using First-Principles Molecular Dynamics Simulations within Generalized Gradient Approximation, Journal of Chemical Theory and Computation, 15, 595-602, 10.1021/acs.jctc.8b00567, 2019.

Perumpully, S. J. and Gautam, S.: Impact of aerosols on atmospheric processes and climate variability: A synthesis of recent research findings, Geosystems and Geoenvironment, 4, 100317, https://doi.org/10.1016/j.geogeo.2024.100317, 2025.

Pillar, E. A., Camm, R. C., and Guzman, M. I.: Catechol Oxidation by Ozone and Hydroxyl Radicals at the Air-Water Interface, Environmental Science & Technology, 48, 14352-14360, 10.1021/es504094x, 2014.

Pino-Rios, R., Inostroza, D., Cárdenas-Jirón, G., and Tiznado, W.: Orbital-Weighted Dual Descriptor for the Study of Local Reactivity of Systems with (Quasi-) Degenerate States, Journal of Physical Chemistry A, 123, 10556-10562, 10.1021/acs.jpca.9b07516, 2019.

Salvador, C. M. G., Tang, R. Z., Priestley, M., Li, L. J., Tsiligiannis, E., Le Breton, M., Zhu, W. F., Zeng, L. M., Wang, H., Yu, Y., Hu, M., Guo, S., and Hallquist, M.: Ambient nitro-aromatic compounds - biomass burning versus secondary formation in rural China, Atmospheric Chemistry and Physics, 21, 1389-1406, 10.5194/acp-21-1389-2021, 2021.

Schaefer, T. and Herrmann, H.: Competition kinetics of OH radical reactions with oxygenated organic compounds in aqueous solution: rate constants and internal optical absorption effects, Physical Chemistry Chemical Physics, 20, 10939-10948, 10.1039/c7cp08571k, 2018.

Shenghur, A., Weber, K. H., Nguyen, N. D., Sontising, W., and Tao, F. M.: Theoretical Study of the Hydrogen Abstraction of Substituted Phenols by Nitrogen Dioxide as a Source of HONO, Journal of Physical Chemistry A, 118, 11002-11014, 10.1021/jp508516c, 2014.

Shi, K., Mei, X. L., Chen, C. R., and Liu, C. Q.: Impact of atmospheric O3 and NO2 on the secondary sulfates in real atmosphere, Journal of Environmental Sciences, 150, 277-287, 10.1016/j.jes.2024.02.019, 2025.

Shirts, M. R., Pitera, J. W., Swope, W. C., and Pande, V. S.: Extremely precise free

energy calculations of amino acid side chain analogs: Comparison of common molecular mechanics force fields for proteins, Journal of Chemical Physics, 119, 5740-5761, 10.1063/1.1587119, 2003.

Shukla, S. S., Dorris, K. L., and Chikkaveeraiah, B. V.: Photocatalytic degradation of 2,4-dinitrophenol, Journal of Hazardous Materials, 164, 310-314, 10.1016/j.jhazmat.2008.08.047, 2009.

Spiegel, M., Semidalas, E., Martin, J. M. L., Bentley, M. R., and Stanton, J. F.: Post-CCSD(T) corrections to bond distances and vibrational frequencies: the power of Λ, Molecular Physics, 122, 10.1080/00268976.2023.2252114, 2024.

Steiner, T.: The Hydrogen Bond in the Solid State, Angewandte Chemie International Edition, 41, 48-76, https://doi.org/10.1002/1521-3773(20020104)41:1<48::AID-ANIE48>3.0.CO;2-U, 2002.

Sun, J., Mu, Q., Kimura, H., Murugadoss, V., He, M., Du, W., and Hou, C.: Oxidative degradation of phenols and substituted phenols in the water and atmosphere: a review, Advanced Composites and Hybrid Materials, 5, 627-640, 2022.

Sun, Y. N., Yao, J. F., Tang, Y. Z., Zhang, Y. J., Wu, W. Z., and Sun, J. Y.: Theoretical study on the atmospheric degradation mechanism and subsequent products of E,E-2,4-hexadienal with hydroxyl radical, International Journal of Quantum Chemistry, 121, 10.1002/qua.26563, 2021.

Sushko, I., Novotarskyi, S., Körner, R., Pandey, A. K., Cherkasov, A., Li, J., Gramatica, P., Hansen, K., Schroeter, T., Müller, K. R., Xi, L., Liu, H., Yao, X., Öberg, T., Hormozdiari, F., Dao, P., Sahinalp, C., Todeschini, R., Polishchuk, P., Artemenko, A., Kuz'min, V., Martin, T. M., Young, D. M., Fourches, D., Muratov, E., Tropsha, A., Baskin, I., Horvath, D., Marcou, G., Muller, C., Varnek, A., Prokopenko, V. V., and Tetko, I. V.: Applicability domains for classification problems: Benchmarking of distance to models for Ames mutagenicity set, J Chem Inf Model, 50, 2094-2111, 10.1021/ci100253r, 2010.

Szatylowicz, H., Jezuita, A., Ejsmont, K., and Krygowski, T. M.: Substituent Effect on the σ- and π-Electron Structure of the Nitro Group and the Ring in Meta- and Para-Substituted Nitrobenzenes, Journal of Physical Chemistry A, 121, 5196-5203,

907 10.1021/acs.jpca.7b03418, 2017.
908 Tam, J. Y. C., Lorsbach, T., Schmidt, S., and Wicker, J. S.: Holistic evaluation of bio-
909 degradation pathway prediction: assessing multi-step reactions and intermediate prod-
910 ucts, Journal of Cheminformatics, 13, 63, 10.1186/s13321-021-00543-x, 2021.
911 Thangamani, D., Shankar, R., Vijayakumar, S., and Kolandaivel, P.: Mechanism and
912 kinetics of the atmospheric degradation of 2-formylcinnamaldehyde with O_3 and hy-
913 droxyl OH radicals - a theoretical study, Molecular Physics, 114, 3055-3075,
914 10.1080/00268976.2016.1214293, 2016.
915 Tiwari, J., Tarale, P., Sivanesan, S., and Bafana, A.: Environmental persistence, hazard,
916 and mitigation challenges of nitroaromatic compounds, Environmental Science and
917 Pollution Research, 26, 28650-28667, 10.1007/s11356-019-06043-8, 2019.
918 Tomas, A., Olariu, R. I., Barnes, I., and Becker, K. H.: Kinetics of the reaction of O3
919 with selected benzenediols, International Journal of Chemical Kinetics, 35, 223-230,
920 https://doi.org/10.1002/kin.10121, 2003.
921 Tuñón, I. and Williams, I. H.: Chapter Two - The transition state and cognate concepts,
922 in: Advances in Physical Organic Chemistry, edited by: Williams, I. H., and Williams,
923 N. H., Academic Press, 29-68, https://doi.org/10.1016/bs.apoc.2019.09.001, 2019.
924 Tyburski, R., Liu, T. F., Glover, S. D., and Hammarström, L.: Proton-Coupled Electron
925 Transfer Guidelines, Fair and Square, Journal of the American Chemical Society, 143,
926 560-576, 10.1021/jacs.0c09106, 2021.
927 Van Der Spoel, D., Lindahl, E., Hess, B., Groenhof, G., Mark, A. E., and Berendsen, H.
928 J. C.: GROMACS: Fast, flexible, and free, Journal of Computational Chemistry, 26,
929 1701-1718, https://doi.org/10.1002/jcc.20291, 2005.
930 vom Eyser, C., Börgers, A., Richard, J., Dopp, E., Janzen, N., Bester, K., and Tuerk, J.:
931 Chemical and toxicological evaluation of transformation products during advanced ox-
932 idation processes, Water Science and Technology, 68, 1976-1983,
933 10.2166/wst.2013.452, 2013.
934 Wang, C. L., Zhao, N., Ma, Z. J., He, M. X., Hou, C. X., and Sun, J. F.: Unraveling the
935 heterogeneous reaction of 4-nitrocatechol with ozone in the atmosphere:A combined
936 DFT, molecular dynamics, and environmental risk assessment, Atmospheric Research,

331, 10.1016/j.atmosres.2025.108632, 2026.

Xing, L., Wu, J., Elser, M., Tong, S., Liu, S., Li, X., Liu, L., Cao, J., Zhou, J., El-Haddad, I., Huang, R., Ge, M., Tie, X., Prévôt, A. S. H., and Li, G.: Wintertime secondary organic aerosol formation in Beijing–Tianjin–Hebei (BTH): contributions of HONO sources and heterogeneous reactions, Atmos. Chem. Phys., 19, 2343-2359, 10.5194/acp-19-2343-2019, 2019.

Yan, J. P., Wang, X. P., Gong, P., and Wang, C. F.: Nitrated polycyclic aromatic compounds in the atmospheric environment: A review, Critical Reviews in Environmental Science and Technology, 51, 1159-1185, 10.1080/10643389.2020.1748486, 2021.

Yang, B., Ren, P. P., Xing, L., Wang, S. H., and Sun, C. L.: Roles of hydrogen bonding interactions and hydrophobic effects on enhanced water structure in aqueous solutions of amphiphilic organic molecules, Spectrochimica Acta Part a-Molecular and Biomolecular Spectroscopy, 296, 10.1016/j.saa.2023.122605, 2023a.

Yang, B. R., Liang, A. B., and Wang, L. M.: The atmospheric oxidation mechanism of acetophenone initiated by the hydroxyl radicals, Atmospheric Environment, 309, 10.1016/j.atmosenv.2023.119905, 2023b.

Young, D., Martin, T., Venkatapathy, R., and Harten, P.: Are the Chemical Structures in Your QSAR Correct?, Qsar & Combinatorial Science, 27, 1337-1345, 10.1002/qsar.200810084, 2008.

Zhao, Y. and Truhlar, D. G.: The M06 suite of density functionals for main group thermochemistry, thermochemical kinetics, noncovalent interactions, excited states, and transition elements: two new functionals and systematic testing of four M06-class functionals and 12 other functionals, Theoretical Chemistry Accounts, 120, 215-241, 10.1007/s00214-007-0310-x, 2008.